Optical and Electrical Performance Analysis of InGaAs/InP Laser for Various Crystal Orientations

Marwa M. Ismaeel[1] and Maad M. Mijwil[2]

[1] Computer Techniques Engineering Department, Baghdad College of Economic Sciences University
Baghdad, Iraq
Email: marwa_mustafa [AT] baghdadcollege.edu.iq

[2] Computer Techniques Engineering Department, Baghdad College of Economic Sciences University
Baghdad, Iraq
Email: mr.maad.alnaimiy [AT] baghdadcollege.edu.iq

ABSTRACT— ***The optoelectronic achievement of a lattice matching InGaAs/InP lateral cavity surface radiating LASER in crystal orientations (100), (110), (111), (113), and (131) is computationally simulated utilising MATLAB by attempting to solve a k.p Hamiltonian of eight-band utilising only a finite difference strategy with spin-orbit linkage. To shift wave-vector k as well as Hamiltonian from traditional (100) plane orientation, tensor plane revolution equations are used. It is demonstrated that optical emission spectrum and crystal plane alignments have a significant correlation. At a carriers injection density of 2.50 x 1018 per cm3, the maximum and minimum gains are measured in the (111) as well as (100) orientations, respectively, with optimum emission wavelengths of 1770.00nm and 1680.00nm. This research will serve as a catalyst for the development of ultra-fast optoelectronic devices with improved performance thanks to the use of non-100 orientation epitaxial layers.***

Keywords— QW-VCSEL, Optic-fiber communication, Crystal orientation, Hamiltonian matrix.

1. INTRODUCTION

Due to their controllable energy band-gap, strong electron mobility, improved exaction-binding energies throughout quantum wells (QW), as well as much lower appearance of piezoelectric (PZ) regions and associated quantum confinement stark effect (QCSE), III-V semiconductor zinc blende (ZB) trio but instead alloys containing quaternary elements were used thoroughly for higher efficiency applications in optoelectronics such as laser diodes and LED along with for electronic mode of transportation [1]. Near-infrared (NIR) lasers with an active area formed of III(Al,Ga,In)-V(P,As,Sb,N) ZB composite alloys but also oscillating at around 1.50 ~ 2.00 μm wavelength have piqued interest because of their wide range of applications throughout healthcare science (eye surgery), LIDAR (light detection and ranging), gas (CO2/NOx) suspecting, optical communications, hyper-spectral image analysis, and security[2–4]. According to recent research, 2.0 μm laser emission is beneficial for accurate surgery in Urology, Gynecology, and Neurology [5,6]. Antimonite semiconductor lasers were shown amongst 2.0 μm and 3.3 μm, however because of the strong miscibility gap and slow recombination, attaining high power has proven difficult [7–9]. conversely, the InGaAs/InP system's mature fabrication technique and strong thermal conductivity enable it acceptable for single phase lasing emissions in the 2.0 – 2.5 μm wavelength spectrum [10–12].

It is generally known that lasers' optical gain as well as threshold current profile could be enhanced by adding a compressively stretched QW inside the active site [13]. Crystal orientation affects the dispersion of energy bands of fracturing strained QW, specifically the energy gap between the valance sub-bands, which results to variations in states density and efficient mass of an electron [14]. Even though (100)-oriented progress produces good crystalline reliability QWs and PZfield has no effect on with the strain values that same orientation indicated, performance in quantum but instead optical gain are perceived as being reduced, owing to the lower charge carriers' transition capability amongst the conduction band as well as the valence band at the gamma (Γ)-point, which is partly because of minimized energy partitioning amongst valence sub-bands [15]. Lasing emission is largely determined by gaps in energy bands including curvature of band at the -point. Crystal orientation is an important parameter to adjust the optoelectronic properties and electrical spectra of a straining ZB QW laser in addition to improve its efficiency [14,15]. The latest fabrication methods, MOCVD (Metal-Organic Chemical Vapor Deposition) and MBE (Molecular BeamEpitaxy), propose crystal formation in an unconventional orientation. For the first time, optical anisotropy throughout ZB type-II(110)-oriented GaAsSb/GaAs was examined using efficient mass theory [16]. The impact of substrate orientations on formation of InSb nanostructures

were established in a study by Chou [17]. Only a few studies have been done on the orientation-centered optoelectronic features of cubic ZB III-N as well as III-V-N QWs. [18] has reported the dispersion of energy band profiles of GaAsBi/GaAs and InGaAsN/GaAs QWs developed on distinct (hhl)-oriented QWs. The structural and electrical features of cubic BN/GaN as well as AlN/GaN super lattices produced in various crystallographic orientations have been studied analytically [19,20]. A comprehensively constrained cubic InGaN QW blue-violet laser as well as an InGaP/GaP QW red laser have indeed undergone crystal orientation-focused optoelectronic investigation [21,22]. Furthermore, little research was done on the critical features of ZB III-V QW structure that are reliant on crystal orientations. Anisotropy, piezoelectricity, and crystalline structure have all been examined as influences on phonon acoustics oscillations in GaAs/AlAs superlattices including GaAs QW slabs [23,24]. They described a generic numerical approach for determining photoelastic factors in (hkl)- orientated cubic crystal structures [25]. PZ fild-focused energy band structural properties and optical gain characteristic of (111)-oriented AlGaInAs/InP multi-QW structure for NIR laser application domains are demonstrated and examined using a self-optimizing genetic algorithm technique [26], which probably holds a lot of promise to select as an alternate solution active area for highly efficient NIR lasers. It would have been fascinating to explore how such an InGaAs/InP QW laser architecture produced along the (hkl) crystal orientation outperforms a normal (100)-dependent crystalline structure in just this regard. For NIR InGaAs/InP QW lasers, orientation-focused light emitting spectra and subsequent outcome energy and frequency response situations were not thoroughly investigated.

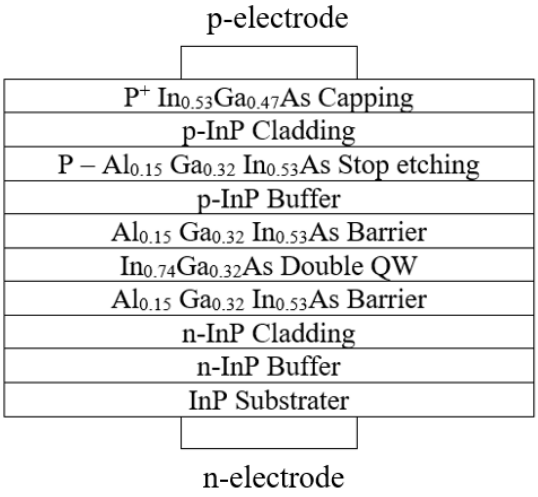

Figure 1: NIR laser architecture of InGaAs-InP laser [27]

The lasing power as well as the steady-state frequency responsiveness of a 1.60% collation strained $In_{0.74}Ga_{0.26}As/A_{10.15}Ga_{0.32}$ $In_{0.53}As$ NIR laser in indeterminate (hkl) crystal alignments have been determined via theoretical modelling utilising an 8-band k.p matrix. The rotation of Euler's tensor approach is used to convert Hamiltonian's eight bands using (100) crystal alignments to acquire the prominent attributes in non-conventional crystalline orientations. Again, for suggested laser structure, finite differences are used to calculate the Eigen energies but also wave functions of the valence and conduction bands. The emission spectra are calculated using electron transition probability and wave functions. An identical model circuit is constructed in MATLAB utilizing laser rate formulas with three levels to obtain output power vs. injected current features. In the MATLAB environment, the frequency response is calculated using a bode plot. At 300 K, the results described here were obtained.

2. RESOURCES AND COMPUTATIONAL PARTICULARS

2.1 LASER Structure

Figure 2 shows a laser system with a 10nm $In_{0.53}$ $Ga_{0.47}$ As effective layer linked by 7nm InP barrier layers and a projecting layer of wide bandgap GaInAsP. As reflectors, two $A_{10.05}$ $Ga_{0.42}$ $In_{0.53}$ As/ InP DBRs with a mean reflectance of 99.50% are utilized. The GaAs substrate is used to grow all of the layers. The h, k, and l components of the active area are modified in a non-orthodox (hkl)-oriented laser architecture. As just a function of material constitution, the energy gap, E_g for such a well plus barrier, is provided by [29]:

$$E_g(In_xGa_{1-x}As) = (1-x)E_g^{GaAs}(T) + xE_g^{InAs}(T) - 0.58x(1-x) \quad (1)$$

$$E_g\left(Al_xGa_yIn_{1-x-y}As\right) = xE_g^{AlAs}(T) + yE_g^{GaAs}(T) + (1-x-y)E_g^{InAs}(T) \quad (2)$$

In "(1)" and "(2)", $E_g^{GaAs}(T)$, $E_g^{InAs}(T)$ and $E_g^{AlAs}(T)$ regarding GaAs, InAs, and AlAs epi layers, characterise the semiempirical non-linear relationship of band gaps upon temperature T (band gap shrinking (BGS)). Equation "(3)" describes this temperature dependence. [30].

$$E_g = E_g(T = 0K) - \zeta\Theta p\left[\frac{1-\chi}{\left(\frac{\Theta p}{T}\right)-1} + \frac{\chi}{4}\left(\sqrt[4]{1+\frac{\pi^2}{6}\left(\frac{4T}{\Theta p}\right)^2+\left(\frac{4T}{\Theta p}\right)^4}-1\right)\right] \quad (3)$$

Where, ζ= Coefficient of bandgap temperature, χ = phonon dispersal degree and Θp = phonon temperature.

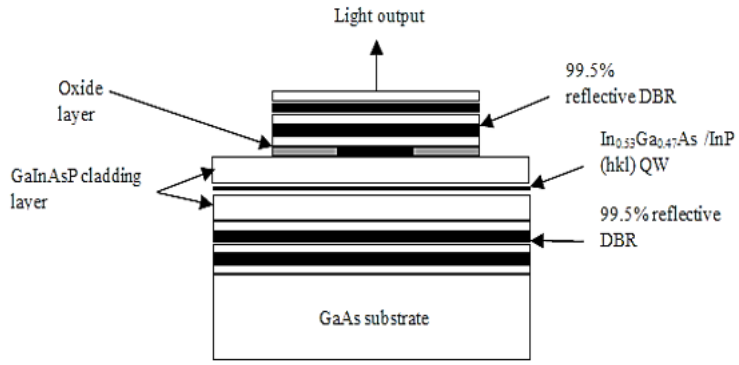

Figure 2: InGaAs/InP lattice-matched architecture [28]

2.2 Optical Gain and Crystal Orientation-Dependent Energy Band Schematic

An 8 × 8 k•p perturbations matrix is used to calculate energy band of the laser structure's schematic. The crystal orientation (1 0 0) adjusted Kane 8 × 8 matrix is provided by [31]:
An 8 × 8 k•p perturbation matrix is used to analyze the laser structure's energy band schematic. [31] gives the updated Kane 8 × 8 matrices for crystallographic orientation (1 0 0):

Parameters

```
h_planck=6.62606896e-34; %% Planck constant [J.s]

hbar=h_planck/(2*pi); %% reduced plancks constant

e=1.602176487E-19; %% charge de l electron [Coulomb]

m0=9.10938188E-31; %% electron mass [kg]

H0=hbar^2/(2*m0);

gc = 1+2*F;


Calculation of Matrix element
B =0;

A =Ec + gc*H0 * (kx.^2 + ky.^2 + kz.^2);

U = sqrt(1/3) * P0 * kz;

V = sqrt(1/6) * P0 * (kx - 1i*ky);

W = 1i*sqrt(1/3)*B * kx*ky;

T = sqrt(1/6)*B * kz*( kx + 1i*ky);

P = -γ1*H0 * (kx.^2 + ky.^2 + kz.^2);

Q = -γ2*H0 *(kx^2 + ky^2 - 2*kz^2);

R = -H0 * sqrt(3)*(γ2*(kx^2-ky^2)-2i*γ3*kx*ky );

S = H0 *2*sqrt(3)*γ3*(kx-1i*ky)*kz;

Hdiag = [A A P-Q P+Q P+Q P-Q -delta+P -delta+P]; % Hamiltonian diagonal element
```

$$H = \begin{bmatrix} 0 & 0 & T' + V' & 0 \\ 0 & 0 & \text{sqrt}(2) * (W - U) & -\text{sqrt}(3) * (T' + V') \\ 0 & 0 & 0 & -S' \\ 0 & 0 & 0 & 0 \\ 0 & 0 & 0 & 0 \\ 0 & 0 & 0 & 0 \\ 0 & 0 & 0 & 0 \\ 0 & 0 & 0 & 0 \end{bmatrix}$$

$$\begin{bmatrix} \text{sqrt}(3) * (T - V) & \text{sqrt}(2) * (W - U) \\ 0 & (T - V) \\ R & 0 \\ 0 & R \\ 0 & S' \\ 0 & 0 \\ 0 & 0 \\ 0 & 0 \end{bmatrix}$$

$$\begin{bmatrix} (W - U) & \text{sqrt}(2) * (T' + V') \\ -\text{sqrt}(2) * (T - V) & W' + U \\ \text{sqrt}(3/2) * S & \text{sqrt}(2) * Q \\ -\text{sqrt}(2) * R & \text{sqrt}(1/2) * S \\ \text{sqrt}(1/2) * S' & \text{sqrt}(2) * R' \\ -\text{sqrt}(2) * Q & \text{sqrt}(3/2) * S' \\ 0 & 0 \\ 0 & 0 \end{bmatrix}$$

H=H'+H+diag(Hdiag); %H' is H_transpose

P0 is the interaction amongst the conduction as well as valence bands, Ec & Ev are really (unstrained) conduction as well as valence band energies, γi's are updated Luttinger parameters, and Ec & Ev are really the (unstrained) conduction & valence band energies, correspondingly. Through diagonalizing the Hamiltonian and to use a quantitative finite difference technique, the energy dispersion profile across (100) orientation is illustrated as a function of k for such 8-band k.p hypothesis. P0 denotes the coupling amongst the conduction as well as valence bands, Ec and Ev denote the (unstrained) conduction plus valence band energies systematically, Δ is split of the spin orbit and γi's denotes the modified Luttinger parameters, Δ is the separation of the spin orbit, the Ec and Ev denote the (unstrained) conduction and valence band energies, correspondingly. By diagonalizing the Hamiltonian employing a quantitative finite difference technique, the energy dispersion characteristic along (100) orientation again for 8-band k.p theory is depicted as a function of k.

2.3 Wave Vector Dependent on Crystal Orientation

The wave vectors over (100) crystal could be predicted by the given formula if the operative channel is developed on (hkl) crystalline orientation [32]:

$$\begin{pmatrix} k_1 \\ k_2 \\ k_3 \end{pmatrix} = O_R \begin{pmatrix} k_x \\ k_y \\ k_z \end{pmatrix}$$

The rotation matrix's formulation is as shown in [33]:

$$O_R = \begin{pmatrix} cos\theta cos\varphi & -sin\varphi & sin\theta cos\varphi \\ cos\theta sin\varphi & cos\varphi & sin\theta sin\varphi \\ -sin\theta & 0 & cos\theta \end{pmatrix}$$

Where $\theta = tan^{-1}\left(\frac{\sqrt{(h^2+k^2)}}{l}\right)$ and $\varphi = tan^{-1}\left(\frac{k}{h}\right)$

The Hamiltonian matrix with (100) crystallographic orientation could be constructed using the wave vector mostly in (100) crystal orientation, as shown in Matrix H. The simple formula could then be used to enumerate the Hamiltonian matrix in orientations:

$H^{hkl} = UH^{(100)}U^*$

Where $U = R(\theta)R(\varphi)$

The rotations that convert the (100) oriented valence band Hamiltonian towards the arbitrary crystal oriented Hamiltonian matrix have been denoted by and in this formulation. The arguments of could be defined as follows:

$$R(\theta) = \begin{pmatrix} \alpha^2 & -\sqrt{3}\alpha^2\zeta & \sqrt{3}\alpha\zeta^2 & \zeta^3 \\ \sqrt{3}\alpha^2\zeta & \alpha^3 - 2\alpha\zeta^2 & -2\alpha^2\zeta + \zeta^3 & \sqrt{3}\alpha\zeta^2 \\ \sqrt{3}\alpha\zeta^2 & 2\alpha^2\zeta - \zeta^3 & \alpha^3 - 2\alpha^2\zeta & -\sqrt{3}\alpha^2\zeta \\ \zeta^3 & \sqrt{3}\alpha\zeta^2 & \sqrt{3}\alpha^2\zeta & \alpha^3 \end{pmatrix}$$

$\alpha = cos\frac{\theta}{2}$ and $\zeta = -sin\frac{\theta}{2}$

$$R(\theta) = \begin{pmatrix} e^{i(3/2)\varphi} & 0 & 0 & 0 \\ 0 & e^{i(1/2)\varphi} & 0 & 0 \\ 0 & 0 & e^{-i(1/2)\varphi} & 0 \\ 0 & 0 & 0 & e^{-i(3/2)\varphi} \end{pmatrix}$$

2.4 Optical Gain

The optical gain of a quantum well architecture as a function of energy could be estimated by [34]:

$$g(E) = \frac{2q^2h}{n\epsilon_0 cm_0^2 LE} * \sum_{n,m} \int_0^\infty \frac{k_t M_{nm}(k_t)\Gamma/(2\pi)}{(E_{cn}(k_t) - E_{kpm}(k_t) - E)^2 + (\Gamma/2\pi)^2} (f_c^n - f_v^m) dk_t \qquad (4)$$

In strained quantum well architects, q stands for free electron charge, r lowered Planck constant, ε0 just like free space dielectric constant, n like index of refraction, c as speed of light, Ecnas the nth conduction sub-bands, E as photon energy, E kpmas the mth valence sub-bands, and M nm as momentum matrix element. The photon relaxation time is equal toΓ $= \frac{h}{\tau}$; The Fermi levels of conduction as well as valence band are Fc, Fvar. The transition's momentum matrix element could be expressed as

$$M_{nm}(k_t) = \frac{3}{4}\left[\langle \Psi_{n(k_t=0)} | g_m^{(1)} \rangle^2 + \frac{1}{3}\langle \Psi_{n(k_t=0)} | g_m^{(2)} \rangle^2\right] M_b^2 \qquad (5)$$

$$\langle \Psi_{n(k_t=0)} | g_m^{(1)} \rangle = \int_{-\infty}^{\infty} \Psi_{n(k_t=0)}(z) g_m^{(1)}(z) dz \qquad (6)$$

The bulk averaged crystal momentum matrix (Eg=band gap and Δ = split-off band separation) is denoted by Mb:

$$M_b = \left(\frac{m_0}{m_e} - 1\right) \frac{m_0 E_g (E_g + \Delta)}{6\left(E_g + \frac{2}{3}\Delta\right)} \qquad (7)$$

3. RESULTS AND DISCUSSION

The simulation was performed at ambient temperature in a MATLAB software. Figure 3 (a)-(e) shows the valence band dispersion curves during the first Brillouin zone observed in crystal orientations (100), (110), (111), (113), and (131), whereby HH, LH, SH, but also CB denote heavy hole, light hole, spin-orbit split off hole bands, with conduction band, respectively. These figures are presented with relation to the wave vector at about the identical scale to evaluate the orientation dependent energy. The rising conduction and spin-orbit splitted band couplings present considerable anisotropy of uppermost valence band structure across (110) but also (111) orientations with values of k≠0 (plain direction wave vector). The authorized shift from conduction band (C) to HH causes lasing activity. Certain transitions, including such intra-subband transitions, are prohibited because they lower the laser's gain. The transition probability amongst HH and LH is the largest among intra-subbands, but it decreases as the energy separation amongst them increases.

Figure 3 shows the dispersion of energy bands profiles (E-k graph) for crystal orientations (100), (110), (111), (113), and (131) calculated to use a Hamiltonian matrix with eight bands having spin–orbit interactions and presented with the identical scale on the X and Y axes. Since efficient mass of an electron is essentially isotropic and also electrons have a spherical shape symmetrical Eigen-function, the conduction band (CB) is considered to be parabolic all through computation. As shown in Figure 3, the topmost valence band profiles along nonconventional crystal orientations reveals substantial asymmetries due to the strong interaction amongst conduction and three-valence sub-bands. It's well acknowledged that -valley energy splitting in the E-k diagram plays a significant role in laser light emission. For generating spectrum of optical gain, CB-heavy hole (HH) and HH light hole (LH) bands have different energy dispersion now at band boundaries (k = 0) is determined and presented in given Table 1 with relation to the crystal growth angles with reference to the primitive z-axis. CB and HH have the maximum and minimum energy splittings of 0.6170 eV and 0.5440 eV, respectfully, for crystal orientations (113) and (111). Based on the highest energy spacing of 0.3600 eV amongst HH and LH, the valence inter-bands bonding is observed to be lowest for (1 1 1). By this distinguishing feature, the optoelectronic effectiveness of NIR InGaAs/InP lasers along the (111) growth plane is projected to outperform ordinary (100) crystals in terms of optical gain with output power. It has been discovered that energy gap among both HH and LH for (111) orientation, causing variations in m*, mass of an electron and hole, changing the uppermost curve of valence sub-bands as well as the emission profile. The energy gap between the C-HH and HHLH bands is estimated from the energy band dispersion to describe wavelength dependency of maximal emission wavelength. With crystal plane orientations, the energy difference amongst conduction band minimum and valence band maximum changes. For this laser, the intra-band blending impact is negligible in (111) orientation, as shown in table 1. The construction of (110) orientated VCSEL is a significant potential due to the facile MOVPE growth.

Table 1: Separation of energy based on orientation

Crystal Orientation	C-HH (ev)	CB-HH (ev)	HH-LH (ev)
100	0.738	0.560	0.03
110	0.794	0.601	0.17
111	0.702	0.544	0.20
113	0.782	0.617	0.10
131	0.714	0.582	0.07

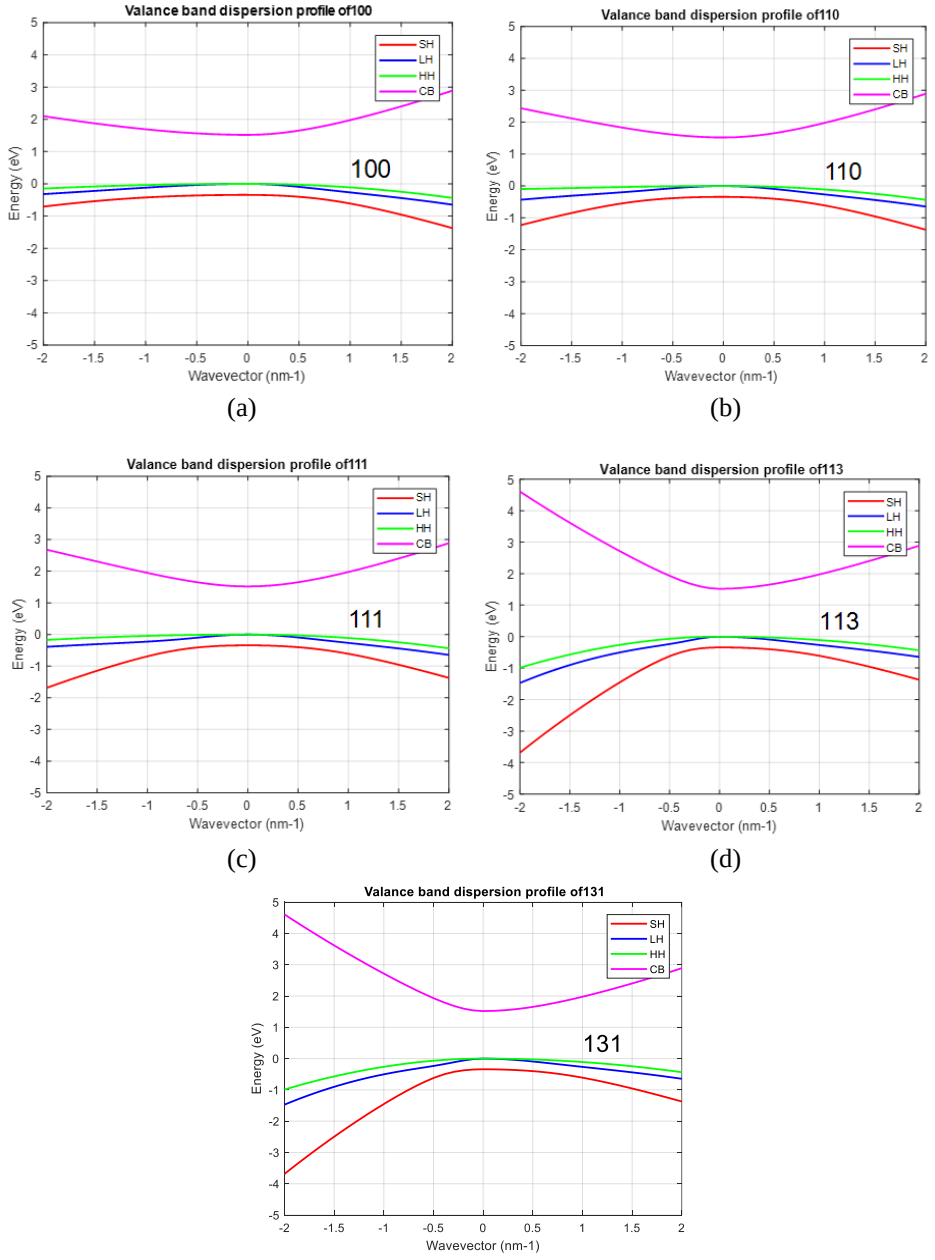

Figure 3: (a). Valence band dispersal pattern of 100 orientated InGaAs/InP Laser, **(b).** Valence band dispersal pattern of 110 orientated InGaAs/InP Laser, **(c).** Valence band dispersal pattern of 111 orientated InGaAs/InP Laser, **(d).** Valence band dispersal pattern of 113 orientated InGaAs/InP Laser, **(e).** Valence band dispersal pattern of 131 orientated InGaAs/InP Laser

The elements of the momentum matrix that really are depending on overlapped wave functions of electron - hole pairs can disclose the orientation dependant peak gain. Figure 4 depicts that transition probability is highest in the (111) orientation and lowest in the (113) and (131) orientations. The enhanced outcome is due to the lowest band gap with minimal intra-band interactions (111). We estimated the optical gain spectra in several crystals orientations employing Eq. (4), as seen in Figure 5, and found that the estimated gains in (100), (110), (113), and (131) orientations are 3800 cm^{-1}, 4600 cm^{-1}, 5400 cm^{-1}, 5000 cm^{-1}, and 4000 cm^{-1}, respectfully. The largest gain is found in the (111) crystal orientation,

whereas the lowest gain is found in the (100) crystal orientation. Because of the small band mixing impact and higher transition probability, the maximum gain is attained in the (111) crystalline orientation. Lowest gain is obtained in (100) crystal orientation for this comparable issue. The highest emission wavelengths for (100), (110), (111), (113), and (131) crystalline orientations are 1.52m, 1.53m, 1.48m, 1.49m, and 1.47m, respectively. With a variation in plane orientation from (100) towards (110), maximal emission spectra (λ) could be altered from 1680.0 nm through 1770.0 nm (111). The energy differential between the C to HH bands is what causes tuning. Furthermore, C-HH band gap is 0.7940 eV in (111), indicating a wavelength of lasing emission of 1.55m that meets the minimal chromatic dispersal limit of OFC. The use of a laser system results in exceptional performance. In addition, the laser produces at 1550nm in (110) directed growth.

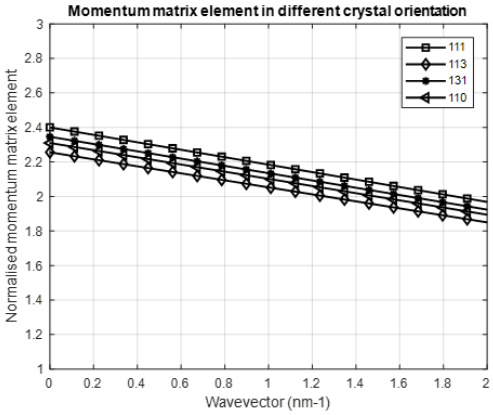

Figure 4: Various crystal orientations of the momentum component

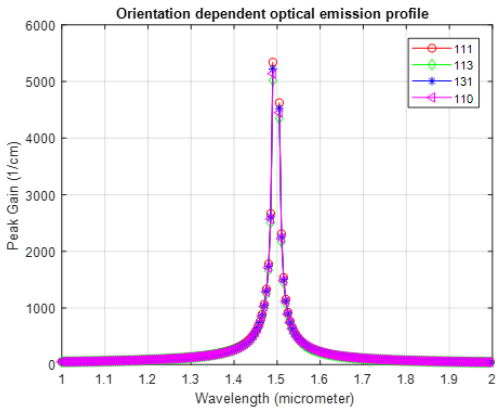

Figure 5: Orientation reliant optical emission profile

4. CONCLUSIONS

The conceptual results show how the energy band dispersion pattern of the conduction and valence bands varies with crystallographic orientation. In the (111) orientation, larger splitting amongst both the heavier hole and lighter hole bands is observed because too little contact from the distant band. The highest optical gain is determined as 5400 cm-1 since the highest values of the momentum component is also tested in this direction. The optimum emission wavelength could be adjusted between 1680 and 1770 nm by altering crystal orientation from (100) to (111). This is the outcome of the (111) and (110)-oriented studies. InGaAs/InP VCSE QW Laser is promising material for fabricating devices for high-speed optoelectronics in optical fiber communication minimal dispersion band. The 1-D Schrodinger formulas for conduction as well as valence bands are computed by discretization with finite elements of such a k.p Hamiltonian matrix with eight bands in addition to study electronic band structures in different orientation. For rotational a (100)-oriented Hamiltonian into another orientation, Euler's tensor rotation equation is used. Crystal orientation affects the energy gap between the conduction as well as valence sub bands. Due to the obvious lowest heavier hole effectual mass, less influence of interior piezoelectric polarization region, and quickest transitioning of charge carriers amongst conduction and valence bands, the (111) crystalline orientation achieves lowest cutoff current and optimal optical power output. Furthermore, as function of crystalline angles and quantum constriction stark impact, The maximum emission wavelengths and optical gain parameters variation. In addition, the frequency responsiveness of the (111)-oriented InGaAs/InP quantum well laser suggests that it could be a promising alternative for high-speed but also near-infrared optoelectronics with improved performance uses.

5. REFERENCES

[1] Riedl T, Lindner JKN. Heteroepitaxy of III–V Zinc blende semiconductors onnanopatterned substrates.Nanoscaled Film Layers 2017:83.
[2] Yu P, et al. Research progress of 2–5 μm Mid-Infrared GaSb semiconductormaterials. ApplPhys 2018;8:45–61.
[3] Ghosh A, Roy AS, Das Chowdhury S, Sen R, Pal A. All-fier tunable ring lasersource near 2μm designed for CO2 sensing. Sensors Actuators B Chem 2016; 235:547–53. https://doi.org/10.1016/j.snb.2016.05.128.
[4] Scholle K, Lamrini S, Koopmann P, and Fuhrberg P, "2 μm Laser Sources and TheirPossible Applications," 2010.
[5] Kundrat D, et al. Preclinical performance evaluation of a robotic endoscope fornon-contact laser surgery. Ann Biomed Eng 2020.https://doi.org/10.1007/s10439-020-02577-y.
[6] Adelman MR, Tsai LJ, Tangchitnob EP, Kahn BS. Laser technology and applicationsin gynaecology. J ObstetGynaecol J InstObstetGynaecol 2013;33(3):225–31.https://doi.org/10.3109/01443615.2012.747495.
[7] Jia H, et al. Investigation of localized state emissions in quaternary InGaAsSb/AlGaAsSb multiple quantum wells grown by molecular beam epitaxy. Opt MaterExpress 2020;10(12):3384–92.

[8] Shengwen X, et al. Research progress of 2 μmGaSb-based high powersemiconductor laser. Infrared Laser Eng 2018;47(5).
[9] Jung D, Bank S, Lee ML, Wasserman D. Next-generation mid-infrared sources. J Opt2017;19(12). https://doi.org/10.1088/2040-8986/aa939b.
[10] Weber MJ. Handbook of lasers.CRC Press; 2019.[11] Wang D, et al. Improved performance of InP-based 2.1 μmInGaAsSb quantum welllasers using Sb as a surfactant. ApplPhysLett 2018;113(25). https://doi.org/10.1063/1.5060653.
[11] Al-Muhanna A, Salhi A. Numerical analysis of InGaAs–InP multiple-quantum well laser emitting at 2 μm. OptQuant Electron 2014;46(7):851–61. https://doi.org/10.1007/s11082-013-9796-8.
[12] Chuang SL. Physics of photonic devices. John Wiley & Sons; 2012.
[13] Duggen L, Willatzen M, Lassen B. rystal orientation effects on the piezoelectricfild of strained zinc-blende quantum-well structures. Phys Rev B 2008;78(20).
[14] Hasan MM, Islam MR, Teramoto K. Crystallographic orientation-dependent optical properties of GaInSb mid-infrared quantum well laser. Optik (Stuttg) 2012;123(21):1993–7. https://doi.org/10.1016/j.ijleo.2011.09.021.
[15] Hong W-P, Park S-H. Optical anisotropy in type-II (110)-oriented GaAsSb/GaAsquantum wells. Solid State Commun 2020;314.
[16] Chou CY, Torf A, Pei C, Wang WI. Effects of substrate orientation on the growth ofInSb nanostructures by molecular beam epitaxy.ApplPhysLett 2016;108(19).https://doi.org/10.1063/1.4949486.
[17] Ivashev I. Theoretical investigations of Zinc Blende and Wurtzite semiconductor quantum wells on the rotated substrates. 2016.
[18] Oukli M, Mehnane N, Oukli N, Bouiadjra BB, Belghoul H. Theoretical investigationof the structural and electronic properties of BN/GaNsuperlattices growth alongvarious crystallographic axes. Phys E Low-dimensionalSystNanostruct 2019;114.https://doi.org/10.1016/j.physe.2019.113653.
[19] Mehnane N, Oukli N, Oukli M. First principles investigation of the structural andelectronic properties of (110), (110) and (111) growth axis AlN/GaNsuperlattices.Chin J Phys 2017;55(4):1275–83.https://doi.org/10.1016/j.cjph.2017.06.004.
[20] Islam MM, Sarker S, Hasan M, Islam R. Orientation dependent performance of635nm vertical cavity surface emitting QW red laser. In: 2015 2nd InternationalConference on Electrical Information and Communication Technologies (EICT);2015. p. 304–8.
[21] Sarker MS, Islam MM, Hasan MM, Islam MR. Crystal orientation dependent performance of cubic InGaN QW blue-violet laser. In: 2015 18th International Conference on Computer and Information Technology (ICCIT); 2015. . 167–71. https://doi.org/10.1109/ICCITechn.2015.7488062
[22] Mahler F, Reimann K, Woerner M, Elsaesser T, Flytzanis C, Biermann K. Impact of piezoelectric filds oncoherent zone-folded phonons in GaAs/AlAssuperlattices.Phys Rev B 2019;100(12). https://doi.org/10.1103/PhysRevB.100.121302.
[23] Duggen L, Willatzen M. Acousto-optical phonon excitation in cubic piezoelectric slabs and crystal growth orientation effects. Phys Rev B 2017;95(3):35310. https://doi.org/10.1103/PhysRevB.95.035310.
[24] Pinky LJR, Islam S, Alam MNK, Hossain MA, Islam MR. Modeling of orientation dependent photoelastic constants in cubic crystal system. Mater SciAppl 2014;2014.
[25] Saidi H, Msahli M, Ben Dhafer R, Ridene S. Self-consistent optimization of [111]-algainas/inpmqwsstructures lasing at 1.5.
[26] Roy, Sourav, Kusay Faisal Al-tabatabai, AniruddhaChakraborty, AlamgirKabir, SanwarHossain, Lway Faisal Abdulrazak, AshrafulHossainHowlader, Rafiqul Islam, and B. Hossain. "Numerical Investigation into Optical and Electronic Performance of Crystal Orientation-dependent InGaAs/InP Near-Infrared Laser." Results in Physics (2021): 104353.
[27] Roy, Sourav, MdImtiazKabir, and KM Abdullah Al-Mamun. "Optoelectronic performance of vertical cavity surface emitting InGaAs/InP QW lASER in non-conventional orientation." In 2016 International Conference on Innovations in Science, Engineering and Technology (ICISET), pp. 1-4, IEEE, 2016.
[28] Khomyakov PA, Luisier M, Schenk A. Compositional bowing of band energies and their deformation potentials in strained InGaAs ternary alloys: a fist-principlesstudy. ApplPhysLett 2015;107(6):62104. https://doi.org/10.1063/1.4928539.
[29] Pohl UW. Electronic properties of heterostructures. In: Epitaxy of semiconductors: physics and fabrication of heterostructures. Cham: Springer International Publishing; 2020. p. 115–75.
[30] Yang Y, Gorelov V, Pierleoni C, Ceperley DM, Holzmann M. Electronic band gaps from quantum Monte Carlo methods. Phys Rev B 2020;101(8):85115. https://doi.org/10.1103/PhysRevB.101.085115.
[31] M.M. Hasan, et al., Crystallographic orientation-dependent optical properties of GaInSb mid-infrared quantum well laser, Optik - Int. J.Light Electron Opt. (2011), doi:10.1016/j.ijleo.2011.09.021
[32] DragicaVasileska, Tutorial for semiconductor band structurecalculation, Arizona State University, Tempe, AZ
[33] A. Niwa, T. Ohtoshi, T. Kuroda, Orientation dependence of opticalproperties in long wavelength strained uantum-well lasers, IEEE J.Selected Top. Quantum Electron.1 (1995) 211- 217